Fast and Accurate Data Collection for Macromolecular Crystallography Using the JUNGFRAU Detector

Filip Leonarski[1], Sophie Redford[1], Aldo Mozzanica[1], Carlos Lopez-Cuenca[1], Ezequiel Panepucci[1], Karol Nass[1], Dmitry Ozerov[1], Laura Vera[1], Vincent Olieric[1], Dominik Buntschu[1], Roman Schneider[1], Gemma Tinti[1], Erik Froejdh[1], Kay Diederichs[2], Oliver Bunk[1], Bernd Schmitt[1*], Meitian Wang[1*]

[1] Swiss Light Source, Paul Scherrer Institute, Villigen, Switzerland.

[2] Fachbereich Biologie, Universität Konstanz, Konstanz, Germany

* Correspondence should be addressed to B.S. and M.W. (email: bernd.schmitt@psi.ch; meitian.wang@psi.ch)

This document is the accepted manuscript version of the following article:
Leonarski, F., Redford, S., Mozzanica, A., Lopez-Cuenca, C., Panepucci, E., Nass, K., … Wang, M. (2018). Fast and accurate data collection for macromolecular crystallography using the JUNGFRAU detector. Nature Methods, 15(10), 799-804. https://doi.org/10.1038/s41592-018-0143-7

Abstract

The accuracy of X-ray diffraction data is directly related to how the X-ray detector records photons. Here we describe the application of a direct detection charge integrating pixel-array detector (JUNGFRAU) in macromolecular crystallography (MX). JUNGFRAU features a uniform response on the subpixel level, linear behavior toward high photon rates, and low-noise performance across the whole dynamic range. These features enable accurate data to be recorded at unprecedented speed. Improvements over previous generation detectors in terms of data quality are demonstrated using one of the most challenging phasing methods in MX with both test and real-life examples. We conclude that the adoption of the JUNGFRAU detector would significantly improve the current performance of synchrotron MX beamlines and make them ready for the future synchrotron light sources.

Keywords: Integrating detector, photon-counting detector, charge-sharing, count-rate, macromolecular crystallography, diffraction data collection, data quality, native-SAD phasing.

Macromolecular crystallography (MX) reveals 3D structures and elucidates functions of biomolecules with atomic resolution, which has enabled fundamental contributions to molecular biology and structure based drug discovery[1]. Synchrotron radiation, together with large format 2D detectors have been essential to the success of modern MX[2,3]. In parallel with the evolution of synchrotron sources, several generations of X-ray detectors have been developed, namely image plate (IP)[4], multiwire proportional counter (MWPC)[5], X-ray television detector (TV)[6], charge-coupled device (CCD)[7], and hybrid (pixel-array) photon-counting detector (HPC)[8]. Each generation excelled the previous one in various ways and has made its marked impact on the development of MX techniques. Currently, most MX beamlines are equipped with HPC detectors or have plans to do so.

New generations of X-ray detectors transformed MX data collection strategies as well. The traditional high-dose and coarse-phi slicing data collection strategy adapted for CCD detectors[9,10] has been replaced by the continuous, low-dose and fine-phi slicing strategy taking full advantage of HPC detectors[11,12]. Very recently, the EIGER detector[13,14] allowed including additional data collection protocols in the standard toolbox of state-of-the-art MX beamlines by enabling fast raster scanning[15] and serial crystallography[16].

Among key features of HPC detectors that enabled these previously impossible data collection protocols, very low noise detection and a point-spread response of a single pixel are achieved by counting an incoming photon only in the pixel where it deposits at least 50% of its energy. Thus, photon counters have a negligible readout noise, meaning that the accuracy with which they can make a measurement is limited by calibration, systematic effects and Poisson statistics.

However, there are two intrinsic effects that may lead to photons not being detected by photon-counting devices, namely charge-sharing and pile-up. Charge-sharing results in photon-induced charges spreading into adjacent pixels when photons hit the sensor near to

the border of pixels ("corner effect"). In such situations, the detection (counting) of the photons strongly depends on the threshold settings. The calibration of the threshold becomes less accurate at low photon energies (≤ 8 keV) and a 50% threshold may not be achievable. Therefore, the effects could be detrimental in low energy applications such as native-SAD phasing where the most accurate measurement of intensity is needed. The effect could be mitigated to a certain degree by increasing the pixel size (e.g. 170 μm square in the PILATUS[11]) and by a charge summing and allocation method as implemented in MEDIPIX3[17], respectively. But such measures reduce spatial resolution and count-rate capability.

Pile-up effects occur at high photon rates due to the dead time in the readout electronic circuit, which needs some time to reset before the next photon can be detected. This count-rate dependence of HPC detectors leads to a non-linear response to photon flux and a count-rate correction needs to be applied[18]. A recent development in retriggering technology[19] extends the count-rate capacity of HPC detectors, but does not eliminate the problem. As an added complication, the count-rate correction in its simplest form is only valid with a constant flux of photons. However, in practice no count rate correction is applied for a changing photon rate when a sharp Bragg peak moves through the diffraction condition during a single exposure. These count-rate related issues are usually avoided in MX measurements as these are carried out with an attenuated beam at a low rotation speed. However, the count-rate capability will become acute for the next generation synchrotrons with higher brilliance[20,21].

To further develop detectors for MX, one challenge is how to overcome the aforementioned charge sharing and pile-up effects while maintaining low-noise performance to the single photon level. and a high dynamic range. New developments of charge integrating hybrid pixel detectors could meet such challenge [22,23] ; JUNGFRAU is one of them[24]. Initially

81 developed for XFEL applications[25], JUNGFRAU features direct detection and a dynamic
82 gain switching technology[24]. Instead of counting individual photons by using a threshold,
83 JUNGFRAU measures the total amount of charge accumulated during the integration time,
84 by which it eliminates both the charge-sharing problem and the count-rate limitation entirely.
85 The three separate gains, each for a given charge range, provide both single-photon
86 sensitivity and a high dynamic range, currently limited by the 1.1 kHz frame rate to 12 Mcps
87 pxl^{-1} at 12.0 keV.[26] The gain is switched automatically and independently per pixel
88 depending on the detected charge. The result of this approach is the combination of a linear
89 response up to much higher photon rates and noise well below the limits set by *Poisson*
90 counting statistics. This is illustrated in one recorded Bragg peak from a lysozyme crystal
91 (Fig. 1). In this study, we demonstrate that JUNGFRAU maintains the advantages of HPC
92 detectors for routine MX applications and offers significant improvements for emerging MX
93 applications in low-energy phasing and serial crystallography, and for future diffraction
94 limited storage rings (DLSRs).[20]
95
96 **Results**
97 **JUNGFRAU maintains low-noise performance.** The reliable detection of high-resolution
98 weak reflections is the foremost requirement for X-ray detectors in MX. In this aspect, HPC
99 detectors are near to ideal because of their very low noise detection with single-photon
100 sensitivity and single-pixel point-spread function. To analyze JUNGFRAU's low-noise
101 performance, we compared it with EIGER, a widely used HPC detector, in the most common
102 MX application – native data collection with 12.4 keV X-rays. These two detectors are
103 particularly suited to perform a comparison of photon counting *versus* charge integrating
104 methods since they have the same pixel size, same sensor area, same hybrid nature, and
105 similar sensor thickness. Two data sets were collected with the same thaumatin crystal under

identical X-ray beam conditions (Online Methods) – one with a JUNGFRAU 1Mpixel detector (JF1M; Supplementary Fig. 1) and the other with an EIGER 1Mpixel detector (E1M). The dose was set very low (0.6 kGy / data set) deliberately to have *Poisson* statistics limited noises for the whole resolution range.

The two data sets have almost the same quality with similar R_{meas} (Fig. 2a, Supplementary Table 1 and 2). Both detectors recorded very weak intensities down to the one photon level at resolutions of 2 Å and higher. The half-data set correlations ($CC_{1/2}$), intensities, and I/σ are marginally lower for JF1M because of its slightly reduced duty cycle and thinner Si sensor (Fig. 2b,c,d). After normalizing for detector duty cycle (JF1M 95% *vs.* E1M 99.7%) and sensor thickness (JF1M 320 μm *vs.* E1M 450 μm) (Online Methods), the intensities and I/σ values are virtually the same in the whole resolution range for both detectors (Fig. 2c,d). As the maximum duty cycle of JUNGFRAU will be improved to the 99% level in the future, and since thicker sensors may be chosen during detector construction, it is expected that the performance of JUNGFRAU will approach the excellent results of EIGER for weak diffraction.

JUNGFRAU enables data collection with full flux. To test JUNGFRAU for high count-rate applications, we performed a series of experiments with increasing flux (beam transmission 1, 20, 50, 100%) and rotation speed (1, 20, 50, and 100 ^{o}/s) from a thaumatin crystal at 6 keV (Online Methods). Compare with the previously published similar experiments with an E1M detector, where the data quality gradually deteriorated with increased flux due to count-rate limit[19], the four JF1M data sets were of very similar quality as judged by R_{meas} and I/σ (Fig. 3a,b, Supplementary Table 1and 3) and their intensity correlations are in excellent agreement across the whole dynamic range (Fig. 3c). In the JF1M 100^{o}/s data set, the top 1 and 6 percentile of strong reflections contained data recorded with photon rates of 500 and 200 Mcps mm^{-2}, respectively (Online Methods, Supplementary Table 4), which are beyond or

close to the count-rate limit of typical HPC detectors respectively. The strongest reflection in the dataset (h=1,k=1,l=1) shows that JUNGFRAU operated at 1.136 kHz is capable of measuring photon rates of more than 4,300 Mcps mm^{-2} at an X-ray energy of 6 keV (Fig. 3d).

JUNGFRAU improves data accuracy. A native-SAD phasing experiment was chosen to assess the quality of data obtained with the JUNGFRAU detector because this method relies on very accurate measurements of reflection intensities to derive phases[27,28]. A thaumatin crystal was measured with 6 keV X-rays using both the JF1M and E1M detectors (Online Methods). Two settings were used for the E1M - one with the default 50% threshold (E1M-50), and the other with 60% (E1M-60) to simulate a situation where the lowest possible threshold is higher than 50% of the photon energy (< 6 keV). For the direct comparison, all measurements were made at the same position of the same crystal with identical data collection parameters (Online Methods). For this thaumatin crystal, the typical size of a diffraction spot is few pixels on average and is smaller at low resolution than at high resolution due to the parallax in the diffraction geometry (Supplementary Fig. 2).

The recorded JF1M data are of high quality as evaluated by R_{meas} (Fig. 4a, Supplementary Table 1 and 5) and I/σ (Supplementary Fig. 3). The R_{meas} of 2.5% at the lowest resolution shell reflects the excellent consistency between individual measurements. The R_{meas} gradually increases with the resolution to 5% at 2.7 Å with a characteristic bump around 6 Å due to an intensity distribution typical to most protein crystals. In contrast, the E1M-50 data are noticeably worse at low resolution with R_{meas} of 5%. The data quality further deteriorates in the E1M-60 data. Such differences have a significant impact on the average density in the anomalous difference Fourier map for sulfur atoms (<S_{anom}>, Fig. 4b). The <S_{anom}> is a useful metric for structure solvability in SAD phasing, and a value above 10σ usually indicates sufficient signal for structure solution[29]. The <S_{anom}> values were 10.2σ, 8.9σ, and 8.3σ for 75° using JF1M, E1M-50, and E1M-60, respectively. Two to three times more data

were required to elevate $<S_{anom}>$ above 10σ for E1M data (Fig. 4b). Indeed, the sub-structure was solved using SHELXC/D[30] with merely 60° JF1M data (Fig. 4c) while the same 60° data from E1M-50 failed to produce a structure solution (Fig. 4d).

To understand the origin of the above discrepancy in data quality obtained with JF1M and E1M detectors, we quantified the uniform response in the sub-pixel level by mapping the deviation of intensities in fractional coordinates of one pixel based on the refined position of reflections ($\Delta_{x,y}$). Then an average pixel map was calculated with the normalized $\Delta_{x,y}$ (Online Methods; Eq. 4). In the case of JF1M the pixel map is essentially featureless, indicating no significant bias in intensity measurement regardless of where the reflection was located within the pixel (Fig. 5a), as expected for a charge integrating detector. However, in the case of E1M-50 there is a systematic difference between reflections centered in the middle of a pixel and near to the corners (Fig. 5b), and the magnitude of the effect increases with the detector threshold (Fig. 5c). Since most diffraction spots of the crystal are elongated in the vertical direction (Supplementary Fig. 2), the effect is much stronger in the horizontal direction in the E1M pixel maps. The non-uniformity in EIGER is likely to be attributed to the corner effect, inaccuracy in threshold calibration and count-rate corrections at low energy. To estimate the contribution of these effects on crystallographic R_{meas}, R_{pxl} was introduced as a measure of systematic errors caused by the non-uniformity across pixels by averaging out random errors (Online Methods; Eq. 5). R_{pxl} values are below 1% for JF1M (Fig. 5d). For E1M data, R_{pxl} has a resolution dependent behavior because the detector non-uniformity is more visible for sharp low-resolution spots. It rises gradually from 3 Å towards lower resolution and becomes a main contributor to the higher R_{meas} in the low-resolution range (Fig. 5e,f).

The sub-pixel and inter-pixel uniformity in JF1M was also verified by detector shifting experiments, in which we measured data sets with JF1M shifted by one third and two thirds

of a pixel in a diagonal direction orthogonal to the beam direction. By combining two data sets – one with and one without the JF1M shift, the data accuracy is the same as measured by $<S_{anom}>$, compared to the same amount of data collected with only one detector position (Fig. 5g). In the similar detector shift experiments with E1M, the data accuracy was significantly improved by combining data from two detector positions to average out the non-uniform response within and between pixels in E1M (Fig. 5h,i). This analysis confirms that JUNGFRAU has good uniform responses within pixels, which permits the measurement of reflection intensities with high accuracy even at low X-ray energies and with diffraction peak sizes comparable to the size of the pixel.

JUNGFRAU expedites experimental phasing. Accurate measurement of reflection intensities with high incoming photon rates, made possible by JUNGFRAU, enables efficient usage of the full flux provided by an undulator beamline efficiently for experimental phasing with anomalous diffraction, whose success stringently depends on the data accuracy. We have chosen one of the most challenging phasing methods - native-SAD to demonstrate JUNGFRAU's distinct advantages.

First, we show that a flash of low-energy X-rays of less than a second is sufficient for native-SAD phasing using a thaumatin crystal as the model system. A total of 60^{o} of data were collected from one crystal at 6 keV with a rotation speed of 100^{o}/s. The entire exposure lasted for 0.6 seconds. With this data, all sulfurs were identified readily with SHELXD[30] and the resulting electron density map from CRANK2[31] was of excellent quality (Fig. 6a). The multiplicity of the data set was only 2.1 (Supplementary Table 1 and 6). This serves as another testament that the uniform response of JUNGFRAU allows achieving high data accuracy with minimum averaging.

To probe the limit further, we attempted a native-SAD experiment with 12.4 keV X-rays using a lysozyme crystal. This energy is unfavorable for native-SAD experiment because the

anomalous scattering factor - *f"* of sulfur is only 0.24 e^-. Although the estimated average differences in structure factors of *Friedel* pairs (i.e., *Bijvoet* ratio) was as low as 0.6%, the structure was phased by SHELXC/D/E with a 500^o data set measured in only five seconds (Fig. 6b). In this case, high-resolution data up to 1.15 Å also helped in accumulating weak but significant anomalous signals (Supplementary Table 1 and 6).

Next, we selected the *E. coli* aminopeptidase N (PepN) representing a real-life example. PepN is a 101 kDa protein (891 residues) containing 30 sulfurs, 1 bromine and 1 zinc atom. Because the average diffraction power of PepN is much weaker compared to test proteins like thaumatin and lysozyme, the rotation speed of data collection was limited to 10^o/s to ensure sufficient exposure per diffraction image with a flux of 2.7×10^{11} ph/s at 6 keV. A 600º data set, collected in one minute (Supplementary Table 1 and 6), allowed a straightforward structure solution using SHELXC/D/E (Fig. 6c). If five to ten times more flux would be available, we expect that the same structure could be solved within 5-10 seconds using 50-100^o/s rotation.

Discussion

The diffraction pattern of a macromolecular crystal contains thousands of sharp Bragg peaks with large variations in their intensities. Solving structures, especially by experimental phasing methods, requires accurate measurement of strong Bragg peaks and the atomic features of a structure are determined by precise recording of weak Bragg peaks at high resolution. Measuring strong and weak intensities has different challenges. Ideally a detector should have uniform response across a large surface area on both the pixel and sub-pixel level, high dynamic range with linear response, high sensitivity to the single photon level, single-pixel point spread function and continuous readout. None of the previous generations of detectors had addressed all these requirements satisfactorily. In response to this challenge,

JUNGFRAU uses a charge integrating readout chip and the successful direct detection hybrid pixel detector technology to provide a low noise performance over the whole dynamic range of 10^4 12 keV photons per frame per pixel and a uniform response within and across pixels. From a data accuracy and precision point of view, the requirements are most stringent in experimental phasing because the small anomalous differences ($\leq 1\%$) between Bragg peaks related by *Friedel*'s law and crystal symmetry lead to reliable evaluation of phases. If the size of Bragg spots is comparable to or smaller than the pixel size of the detector, their measurement accuracy will be compromised when measured with detectors with non-uniform sub-pixel response such as HPCs. The smaller the spot is in comparison to the detector pixel size, the more severe the effect will be. In practice, this shortcoming is mitigated conveniently by collecting true high-multiplicity data using a multi-axis goniometer[28], but at a cost of increasing the X-ray dose and thus the radiation damage[32] and experiment time. In this work, we have demonstrated that JUNGFRAU permits an accurate measurement of photons independent of where they land on the detector surface, which allows obtaining highly accurate data, hence achieving experimental phasing with minimum X-ray dose and reduced multiplicity (Fig. 4). Therefore, the JUNGFRAU detector holds great promise, especially for native-SAD phasing using X-rays in the 3-5 keV range where the calibration of HPC detectors is particularly challenging. Furthermore, the measurements can be carried out faster with high flux because JUNGFRAU is not count-rate limited. This unique combination of accuracy and speed was demonstrated using native-SAD experiments (Fig. 6a,b) with a rotation speed of 100^o/s, a speed that was considered of no practical use in the past, but now can be exploited to develop novel data collection strategies.

Time-resolved crystallography with Laue methods was made possible by 3rd generation high-energy synchrotron facilities[33]. However, the Laue methods required large crystals and specialized beamlines. Very recently, the emerging serial synchrotron crystallography (SSX)

has broadened horizons of time-resolved crystallography by introducing novel crystal delivery techniques and automated data collection methods with fast frame-rate detectors[34-37]. To further improve the efficiency of SSX methods and the time-resolution, the available flux density can be increased 100-1000 fold by using wide-bandpass X-rays[38]. Then integrating detectors become indispensable. JUNGFRAU technology meets the challenges nicely and will allow the study of biologically relevant dynamics down to microsecond timescales in a pump-probe fashion at synchrotrons.

There are challenges in implementing JUNGFRAU at MX beamlines. Dark runs (*i.e.* without X-rays) are required to calculate pedestals for each gain and need to be included in the data acquisition sequence with minimum overhead. The raw data need to be corrected and converted to photons before the data volume can be reduced by frame summation. This requires handling high data rates (4 GB/s per 1M pixels) for real time data analysis. The solutions are in active development at the PSI to match the robustness and simplicity of operating HPC detectors. Such challenges are essentially the same for XFEL serial crystallography applications[39-41].

Using common data acquisition protocols and experimental conditions in terms of photon energy, count-rate and sharpness of the diffraction spots, the HPC detector produces data of high quality for the majority of MX applications currently. But pushing the frontiers of method and technology development further, even this latest detector generation has its limitations. In these scenarios, the improvement in data accuracy and data collection speed obtained with the JF1M detector used here is remarkable. The ultimate obtainable data quality from a given crystal depends on many factors, but it is evident that detectors like JUNGFRAU will be pivotal in getting close to this limit. This is a major advancement in the continuous quest for improving MX data quality and will prompt development of low-noise

instruments in the next generation MX beamlines to capitalize on the full potential of the next generation synchrotron sources like DLSRs in the coming decade.

Acknowledgements

We thank C. Tarnus, C. Schmitt and S. Albrecht for the preparation of PepN crystals.

Author contributions

M.W., O.B. and B.S. conceived the research; S.R., A.M., C.L.-C. built and calibrated JF1M detector; A.M., D.B., and R.S. installed JF1M and E1M detectors at beamlines X06SA; F.L., A.M. and E.P. developed diffraction data collection software; L.V. and V.O. prepared samples; F.L., S.R., A.M., E.P., and M.W. collected data; F.L., S.R., K.N., D.O., G.T., E.F., K.D., and M.W. analyzed data; F.L., S.R., O.B, and M.W. wrote the manuscript with contributions from all authors.

Competing financial interests

The authors declare no competing financial interests.

References

1 Jaskolski, M., Dauter, Z. & Wlodawer, A. A brief history of macromolecular crystallography, illustrated by a family tree and its Nobel fruits. *FEBS Journal* **281**, 3985-4009, doi:10.1111/febs.12796 (2014).

2 Duke, E. M. H. & Johnson, L. N. Macromolecular crystallography at synchrotron radiation sources: current status and future developments. *Proceedings of the Royal Society A: Mathematical, Physical and Engineering Sciences* **466**, 3421-3452, doi:10.1098/rspa.2010.0448 (2010).

3 Gruner, S. M., Eikenberry, E. F. & Tate, M. W. in *International Tables for Crystallography* Vol. F Ch. 7.1, 143-147 (2006).

4 Seggern, H. v. Photostimulable x-ray storage phosphors: a review of present understanding. *Brazilian Journal of Physics* **29**, 254-268, doi:10.1590/s0103-97331999000200008 (1999).

5 Howard, A. J. *et al.* The use of an imaging proportional counter in macromolecular crystallography. *Journal of Applied Crystallography* **20**, 383-387, doi:10.1107/s0021889887086436 (1987).
6 Arndt, U. W. X-ray television area detectors. *Synchrotron Radiation News* **3**, 17-22, doi:10.1080/08940889008602568 (1990).
7 Gruner, S. M., Tate, M. W. & Eikenberry, E. F. Charge-coupled device area x-ray detectors. *Rev Sci Instrum* **73**, 2815-2842, doi:10.1063/1.1488674 (2002).
8 Graafsma, H. in *Semiconductor Radiation Detection Systems* (ed Krzysztof Iniewski) Ch. 10, 217-236 (**CRC Press**, 2010).
9 Waterman, D. & Evans, G. Estimation of errors in diffraction data measured by CCD area detectors. *Journal of Applied Crystallography* **43**, 1356-1371, doi:10.1107/s0021889810033418 (2010).
10 Dauter, Z. Data-collection strategies. *Acta Crystallographica Section D Biological Crystallography* **55**, 1703-1717, doi:10.1107/s0907444999008367 (1999).
11 Broennimann, C. *et al.* The PILATUS 1M detector. *J Synchrotron Radiat* **13**, 120-130, doi:10.1107/s0909049505038665 (2006).
12 Mueller, M., Wang, M. & Schulze-Briese, C. Optimal fine phi-slicing for single-photon-counting pixel detectors. *Acta Cryst* **68**, D42-56, doi:10.1107/S0907444911049833 (2012).
13 Dinapoli, R. *et al.* EIGER: Next generation single photon counting detector for X-ray applications. *Nuclear Instruments and Methods in Physics Research Section A: Accelerators, Spectrometers, Detectors and Associated Equipment* **650**, 79-83, doi:10.1016/j.nima.2010.12.005 (2011).
14 Casanas, A. *et al.* EIGER detector: application in macromolecular crystallography. *Acta Cryst* **D72**, 1036-1048, doi:10.1107/S2059798316012304 (2016).
15 Wojdyla, J. A. *et al.* Fast two-dimensional grid and transmission X-ray microscopy scanning methods for visualizing and characterizing protein crystals. *Journal of Applied Crystallography* **49**, 944-952, doi:10.1107/s1600576716006233 (2016).
16 Diederichs, K. & Wang, M. in *Protein Crystallography Methods in Molecular Biology* Ch. 10, 239-272 (2017).
17 Ballabriga, R. *et al.* The Medipix3RX: a high resolution, zero dead-time pixel detector readout chip allowing spectroscopic imaging. *J Instrum* **8**, C02016-C02016, doi:10.1088/1748-0221/8/02/c02016 (2013).
18 Sobott, B. A. *et al.* Success and failure of dead-time models as applied to hybrid pixel detectors in high-flux applications. *J Synchrotron Radiat* **20**, 347-354, doi:10.1107/s0909049513000411 (2013).
19 Loeliger, T. *et al.* in *2012 IEEE Nuclear Science Symposium and Medical Imaging Conference Record (NSS/MIC)* 610-615 (2012).
20 Eriksson, M., van der Veen, J. F. & Quitmann, C. Diffraction-limited storage rings – a window to the science of tomorrow. *J Synchrotron Radiat* **21**, 837-842, doi:10.1107/s1600577514019286 (2014).
21 Denes, P. & Schmitt, B. Pixel detectors for diffraction-limited storage rings. *J Synchrotron Radiat* **21**, 1006-1010, doi:10.1107/s1600577514017135 (2014).
22 Graafsma, H., Becker, J. & Gruner, S. M. in *Synchrotron Light Sources and Free-Electron Lasers* (eds E. Jaeschke, S. Khan, J. R. Schneider, & J.B. Hastings) Ch. 37, 1029-1054 (Springer International Publishing, 2016).
23 Tate, M. W. *et al.* A Medium-Format, Mixed-Mode Pixel Array Detector for Kilohertz X-ray Imaging. *Journal of Physics: Conference Series* **425**, doi:10.1088/1742-6596/425/6/062004 (2013).

24 Mozzanica, A. *et al.* Characterization results of the JUNGFRAU full scale readout ASIC. *J Instrum* **11**, C02047-C02047, doi:10.1088/1748-0221/11/02/c02047 (2016).
25 Chapman, H. N. *et al.* Femtosecond X-ray protein nanocrystallography. *Nature* **470**, 73-77, doi:10.1038/nature09750 (2011).
26 Redford, S. *et al.* First full dynamic range calibration of the JUNGFRAU photon detector. *J Instrum* **13**, C01027-C01027, doi:10.1088/1748-0221/13/01/c01027 (2018).
27 Liu, Q. *et al.* Structures from Anomalous Diffraction of Native Biological Macromolecules. *Science* **336**, 1033-1037, doi:10.1126/science.1218753 (2012).
28 Weinert, T. *et al.* Fast native-SAD phasing for routine macromolecular structure determination. *Nat Methods* **12**, 131-U163, doi:10.1038/nmeth.3211 (2015).
29 Terwilliger, T. C. *et al.* Can I solve my structure by SAD phasing? Anomalous signal in SAD phasing. *Acta Crystallographica Section D Structural Biology* **72**, 346-358, doi:10.1107/s2059798315019269 (2016).
30 Sheldrick, G. M. Experimental phasing with SHELXC/D/E: combining chain tracing with density modification. *Acta Cryst* **D66**, 479-485, doi:10.1107/s0907444909038360 (2010).
31 Skubák, P. & Pannu, N. S. Automatic protein structure solution from weak X-ray data. *Nature Communications* **4**, doi:10.1038/ncomms3777 (2013).
32 Garman, E. F. Radiation damage in macromolecular crystallography: what is it and why should we care? *Acta Crystallographica Section D Biological Crystallography* **66**, 339-351, doi:10.1107/s0907444910008656 (2010).
33 Neutze, R. & Moffat, K. Time-resolved structural studies at synchrotrons and X-ray free electron lasers: opportunities and challenges. *Current Opinion in Structural Biology* **22**, 651-659, doi:10.1016/j.sbi.2012.08.006 (2012).
34 Gati, C. *et al.* Serial crystallography on in vivo grown microcrystals using synchrotron radiation. *IUCrJ* **1**, 87-94, doi:10.1107/s2052252513033939 (2014).
35 Weinert, T. *et al.* Serial millisecond crystallography for routine room-temperature structure determination at synchrotrons. *Nature Communications* **8**, doi:10.1038/s41467-017-00630-4 (2017).
36 Beyerlein, K. R. *et al.* Mix-and-diffuse serial synchrotron crystallography. *IUCrJ* **4**, 769-777, doi:10.1107/s2052252517013124 (2017).
37 Gruner, S. M. & Lattman, E. E. Biostructural Science Inspired by Next-Generation X-Ray Sources. *Annual Review of Biophysics* **44**, 33-51, doi:10.1146/annurev-biophys-060414-033813 (2015).
38 Meents, A. *et al.* Pink-beam serial crystallography. *Nature Communications* **8**, doi:10.1038/s41467-017-01417-3 (2017).
39 Barty, A. *et al.* Cheetah: software for high-throughput reduction and analysis of serial femtosecond X-ray diffraction data. *Journal of Applied Crystallography* **47**, 1118-1131, doi:10.1107/s1600576714007626 (2014).
40 Mariani, V. *et al.* OnDA: online data analysis and feedback for serial X-ray imaging. *Journal of Applied Crystallography* **49**, 1073-1080, doi:10.1107/s1600576716007469 (2016).
41 Zeldin, O. B. *et al.* Data Exploration Toolkitfor serial diffraction experiments. *Acta Crystallographica Section D Biological Crystallography* **71**, 352-356, doi:10.1107/s1399004714025875 (2015).

406 **Figures legends**

407 **Figure 1** Demonstration of the dynamic gain switching of the JUNGFRAU detector. (Left) A
408 diffraction image from a lysozyme crystal measured without beam attenuation at X06SA
409 beamline, SLS was shown. (Middle) Zoom-in on a Bragg peak showing the number of
410 photons detected, where the central pixel was measured in low gain (red), tails of the peak
411 were measured in medium gain (yellow), while the background is measured in high gain
412 (blue). (Right) The relationship between a charge integrated by the pixel and its ADC count
413 output for three gains (high (G0), medium (G1) and low (G2)).

414 **Figure 2** Data quality comparison between JF1M and E1M for routine MX applications. All
415 comparisons are made as a function of resolution. (A) R_{meas} values. (B) $CC_{1/2}$ values. (C) The
416 intensity ($\langle I \rangle_{\text{unmrgd}}$) values with and without normalization for the duty cycle and sensor
417 thickness. The $\langle I \rangle_{\text{unmrgd}}$ values are prior to application of *Lorentz* and polarization
418 corrections. (D) $\langle I/\sigma \rangle_{\text{unmrgd}}$ values.

419 **Figure 3** Comparison of measurements with different photon rates using the JUNGFRAU
420 detector. (A,B) The R_{meas} and $\langle I/\sigma \rangle_{\text{mrgd}}$ values for measurements obtained with beam
421 transmissions at 1%, 20%, 50%, and 100%. (C) The correlation of integrated intensities of
422 reflections measured with beam transmission of 100% with respective intensities measured at
423 1% transmission (Pearson correlation coefficient of 0.98). Blue dots represent reflections
424 with photon-rate > 200 Mcps mm^{-2}. (D) The correlation of the estimated photon rate
425 extracted from the single pixel of a reflection with highest counts between 1% and 100%
426 transmission data sets (Pearson correlation coefficient of 0.93). The spread of the plot comes
427 from the fact that depending on the slicing position of a reflection, the number of photons
428 might differ for the pixel with the highest counts. The orange line represents an ideal linear
429 response. The black curve is the theoretical behavior of a paralyzable counter with dead time

of 280 ns and the horizontal dotted black line marks a corresponding count-rate limit (see Online Methods).

Figure 4 Comparison of 6 keV data from a thaumatin crystal measured with JF1M and E1M detectors (two threshold settings for E1M). (A) The crystallographic R_{meas} as a function of resolution. (B) The anomalous signal ($<S_{anom}>$) as a function of total rotation range. The magenta line represents the threshold for structure solvability. (C) SHELXD sub-structure determination from 200 trials with 60° JF1M data. The correct solution with high CC_{all} and CC_{weak} is marked as a red dot. (D) SHELXD sub-structure determination from 5000 trails with 60° E1M-50 data.

Figure 5 The sub-pixel uniformity characterizations of the JUNGFRAU and EIGER detectors. The left column shows JF1M data, the central column shows E1M-50 data, and the right column shows E1M-60 data. (A, B, C) Pixel maps for low-resolution data (> 10 Å) (Eq. 4). (D, E, F) R_{pxl} (Eq. 5) and crystallographic R_{meas} as a function of resolution. (G, H, I) Measured anomalous signals from combined data sets with and without detector shifts. Reflections flagged as misfit in XDS were included in calculations of the statistics.

Figure 6 Fast native-SAD phasing with an unattenuated beam at both 6 keV and 12.4 keV with JF1M. For each case, results of the substructure search with SHELXD (left) - the correct solutions with high CC_{all} and CC_{weak} are marked as red dots, and the electron density maps (right) are shown. (A) Thaumatin with 60° of data measured in 600 ms at 6 keV. Density map obtained after density modification, automated tracing and refinement with CRANK2. (B) Lysozyme with 500° of data measured in 5 s at 12.4 keV. Density map obtained after density modification and automated tracing with SHELXE. (C) Aminopeptidase with 600° of data measured in one minute at 6 keV. Density map obtained after density modification and automated tracing with SHELXE.

Online Methods

General experiment setup. Experiments were performed at the X06SA protein crystallography undulator beamline, Swiss Light Source, at beam energies of both 12.4 keV and 6 keV. The beam size was adjusted to 80 × 80 μm^2 and the flux for non-attenuated beam was 1.6×10^{12} ph/s and 2.7×10^{11} ph/s for 12.4 and 6 keV, respectively. For 12.4 keV measurements default beamline settings were used, while for 6 keV the monochromator was detuned by 0.002^o to remove higher harmonics. The beamstop was placed 7 mm from the sample, which shadowed reflections with resolution lower than 10 Å for 12.4 keV X-rays. The beamline was equipped with a motorized stage allowing movement of the JUNGFRAU and EIGER detectors in three directions. Sample to detector distance could be changed in the 40-120 mm range, while the two perpendicular directions could be set within 20 mm from the detector center. The motor resolution was 2.5 μm. Crystal centering and EIGER data collection were controlled using the DA+ software[42]. The JUNGFRAU data collection was carried out with customized programs. Life Sciences Reporting Summary is available online.

JUNGFRAU 1M detector characteristics. The unique feature of the JUNGFRAU detector is its dynamic gain switching with three gain levels accommodating both single photon sensitivity and high dynamic range. The JUNGFRAU detector is modular and each module has an active area of 4 × 8 cm^2 with eight application specific integrated circuits (ASIC) and contains ~500,000 pixels of 75 μm pitch. The sensor geometry is identical to that of EIGER. Modules are independent in terms of read-out, each having a dedicated 10 Gb/s Ethernet link and can be arranged into various geometric shapes. Currently silicon of 320 μm thickness is used for the JUNGFRAU sensor. A thicker sensor, such as the 450 μm thick sensor of EIGER, could also be used.

The JUNGFRAU system used in this experiment consisted of two modules, giving a one million-pixel system (JF1M). The gap between the modules, insensitive to X-rays, was estimated at approx. 2.7 mm (36 pixels). The system was operated with 880 μs frame time (1,136 Hz) and 840 μs integration time (*i.e.,* a duty cycle of 95%). This almost continuous mode is very different from the pulse mode used for XFEL applications. The integration time and the frame rate were determined by detector characteristics coupled with the desire to achieve as high a duty cycle as possible. In order to limit the integration of the leakage current, the present maximum frame rate of 1,136 Hz was used, corresponding to a period of 880 μs. 40 μs is required between the end of integration and the start of readout, to move charge through the chip. This leaves an integration time of 840 μs. The readout of the previous frame is then performed during the integration of the next frame. To further reduce the leakage current, the detector was cooled to -12^{o}C. Other parameters, such as the internal ASIC voltages, sensor bias voltage, timings, are standard as also used in XFELs. A dedicated computer was used to control the detector and to store frames during data collection. The frame rate (1,136 Hz) and frame size (1 million pixels in 16-bit) required a wide bandwidth of 2.3 GB/s to prevent frame loss.

The ASIC of JUNGFRAU is designed to keep the readout noise below Poisson statistics and to have single photon sensitivity at energies as low as 2 keV. The readout noise is estimated as 200 electrons for the high gain with an integration time of 840 μs. Operated at an XFEL with an integration time of 10 μs, the noise is reduced to 70 electrons.

The maximum number of counts is determined by the charge range of the low gain. Since the induced charge from a single photon is proportional to its energy, the dynamic range is effectively doubled at 6 keV in comparison to 12 keV. When operated in the 1.1 kHz frame rate, the dynamic range is about 12 and 25 Mcps pxl^{-1} (2100 and 4400 Mcps mm^{-2}) at 12 and 6 keV, respectively and roughly doubles at the foreseen operation frame rate of 2.3 kHz.

JUNGFRAU data format and image processing. The result of each JUNGFRAU measurement is a raw image. For each pixel the gain level (2-bit) and digitized accumulated charge (14-bit) in arbitrary detector units (ADUs) are recorded. To convert the raw signal to photon energy, six constants are needed per pixel - for each of the three gain levels one needs to know the amplification factor, *i.e.* the ratio of arbitrary detector charge units and energy, and the pedestal, *i.e.* the offset corresponding to the pixel's dark output.

Gain values are assumed to be invariant of experimental conditions and have been measured for the JF1M previously[26]. The achieved accuracy of the gain calibration is at about 1% level currently[43]. The pedestal, on the other hand, depends strongly on experimental conditions, especially on the integration time and the sensor temperature. Therefore, dedicated dark measurements were performed before every data set measured with JF1M, consisting of 5000 frames in high gain (1,136 Hz), 1000 in medium gain (500 Hz) and 1000 in low gain (200 Hz). Since a pedestal drift was observed immediately after the detector starts recording, related to the changes in temperature and operation mode for this particularly long integration time, a delay of 10 s was introduced between detector start and shutter opening. Frames measured during this period were used to dynamically track the pedestal but were not used for data processing. Currently, such procedure introduces approx. 60 seconds delay for an experiment. It is expected that much shorter and less frequent measurement would be sufficient, and optimization for efficiency is under study.

Pedestal subtraction and gain conversion were applied on raw images after data collection finished. The energy measured per pixel was converted to a photon count by dividing by the incoming photon energy. Geometric corrections were performed to account for the ~36 pixel gap between the modules, and the multi-size pixels between the ASICs. Finally an optional frame summation was performed. Since result of conversion of ADU to photon counts is not integers, and floating point values are not supported by common crystallography data

processing packages, these values were rounded to integer and final images were saved in the CBF format[44]. Pixels which saturated the highest possible ADU count at the lowest gain were marked as overloads.

EIGER 1M detector. Comparative data were obtained with an EIGER 1M detector (E1M, Dectris Ltd.). The detector consists of two modules each with ~500,000 pixels of 75 μm pitch, *i.e.* the format is directly comparable to the one of the JUNGFRAU 1M detector used for these experiments. The sensor thickness is 450 μm. Images were saved in HDF5 format.

Protein crystal preparation. Lysozyme was dissolved at 50 mg/ml in 50 mM, Sodium Acetate pH 4.5 and crystallized in 5% PEG MME 5000, 2 M NaCl, 50 mM Sodium Acetate pH 4.5, 25% ethylene glycol. Thaumatin was suspended at 50 mg/ml in water and crystallized in 24% Sodium Potassium Tartrate, 100 mM Bis-Tris Propane pH 6.5. Aminopeptidase PepN crystallization was carried out with inhibitor I1 according to the published protocol[45].

X-ray data collection

Low-noise performance. A large thaumatin crystal (Thau1, 480 × 240 × 180 μm^3) was measured at 12.4 keV with a flux of 3.5×10^9 ph/s (0.25% beam transmission). The data sets with full rotation (360^o) were measured at $50\ ^o$/s rotation speed with both JF1M and E1M detectors. The accumulated dose was about 0.6 kGy per data set[46]. The crystal was kept on the goniometer while detectors were exchanged, so both measurements were made with the same position of the crystal and same X-ray beam conditions. The JF1M and E1M detectors were positioned approximately 60 mm from the sample and operated at 1.136 kHz frame rate and 500 Hz, respectively.

Dynamic range study. A thaumatin crystal (Thau2), with a size of 80 × 80 × 80 μm^3 matching the beam size, was measured at 6 keV with JF1M positioned approximately 40 mm from the crystal. Four 360^o data sets were measured with four settings: (1) 100^o/s rotation

speed and 100% beam transmission, (2) 50°/s and 50% transmission, (3) 20°/s and 20% transmission and (4) 1°/s and 1% transmission. Since intensities from (1) and (4) were to be compared, the attenuation factor for (4) was measured with a photodiode and the precise transmission was found to be 1.16%. Therefore, intensities of data with 1% transmission reported in Fig. 3c and 3d were divided by a factor of 1.16.

Frames were summed: by 2 in case of 50% transmission, by 5 in case of 20% transmission and by 100 in case of 1% transmission. This means all data sets have the same X-ray dose and the same angular increment per summed image. The total dose accumulated through the experiment was estimated at less than 0.5 MGy, well below the damaging dose limit for cryo-cooled crystals.

Sub-pixel uniformity study. Measurements were carried out with both JF1M and E1M detectors operated with the same frame rate of 1.136 kHz and positioned 45 mm from the crystal. Two settings were used for the E1M - one with the default 50% threshold (E1M-50), and the other with 60% (E1M-60). The integration time of JF1M and E1M was 840 μs and 877 μs, corresponding to a duty cycle of 95.5% and 99.7%, respectively. A large thaumatin crystal (Thau3) of about 360 × 240 × 240 μm^3 was measured at 6 keV with 15% beam transmission (flux of 2.5×10^{10} ph/s). The same crystal volume was illuminated with the same X-ray beam through the entire experiment.

All diffraction data were collected with 10°/s rotation speed, *i.e.,* step of 0.0088° in 0.00088 second. Five 360° data sets were measured for each detector. The first two runs were performed with the detector in an initial position, the third one with the detector shifted by 25 μm (⅓ pixel) in both X and Y directions from the initial position, the fourth one with the detector shifted by 50 μm (⅔ pixel) in both X and Y directions and final one with the detector shifted by 225 μm (3 pixel) in both X and Y directions the initial position. Only results of the first three experiments are presented. The total dose accumulated through the experiment was

579 estimated at 1 MGy. For data processing images from both detectors were summed by ten, so
580 one frame corresponds to a 0.088° rotation.
581 **Fast native-SAD phasing.** For native-SAD at 6 keV X-ray energy, a beam size of 80 × 80
582 μm^2 and the full flux of 2.7×10^{11} ph/s was used. A thaumatin crystal, with a size matching
583 the beam size (Thau2, 80 × 80 × 80 um^3), was measured for a 360° angular range at 100°/s
584 rotation speed. The frames with 0.088° angular increment were used for data processing
585 directly, without summing. The same setup at 6 keV for an aminopeptidase PepN crystal of
586 100 × 80 × 80 μm^3 in size was used to measure 720° angular range at 10°/s rotation speed.
587 Ten frames were summed to make one image covering 0.088° rotation width.
588 For native-SAD at 12.4 keV, a lysozyme crystal of 80 × 80 × 80 μm^3 in size was used. The
589 lysozyme data set was measured with 100°/s rotation speed and 100% beam transmission (1.6
590 $\times 10^{12}$ ph/s).
591 **X-ray data processing, structure determination and refinement.** MX data quality is
592 dependent on phi-slicing[12,14] and in principle a slower rotation speed allows for finer slicing
593 at a given detector frame rate – which could result in a bias towards slower rotation speeds
594 (up to the point data processing software can correctly account for the extremely weak signal
595 and low background). Therefore prior to data processing, we have performed frame
596 summation to ensure that images obtained at various rotation speeds correspond to a similar
597 rotation angle (0.088° for 1.136 kHz and 0.100° for 1.000 kHz).
598 Frames were processed with XDS[47] software with standard settings. To improve position
599 refinement for the pixel map calculation, the segment refinement feature of XDS was used to
600 account for imprecisions in module positions and the gap size in JF1M and E1M. To allow a
601 direct comparison of intensities for the dynamic range and low-noise performance
602 experiments, scaling factors for integration in XDS were fixed to 1.0. Intensities calculated in

603 the XDS_ASCII.HKL were divided by the Lorenz-polarization correction factor, to recover
604 the total photon count of a reflection for presentation on Fig. 2c.
605 The calculation of data quality indicators (R_{merge}, R_{meas} and $\langle I/\sigma \rangle$) was performed based on
606 XDS and XSCALE outputs using custom python scripts for plotting in finer resolution shells.
607 In the low-noise performance experiment, the normalization of intensity was calculated with
608 the ratio of the duty cycles and the ratio of the absorptions of Si sensor at 2θ of 32° (Fig. 2c).
609 The I/σ was normalized with the square root of the ratios (Fig. 2d). The duty cycle and sensor
610 thickness are 95% and 99.7% and 320 µm and 450 µm for JF1M and E1M, respectively.
611 Experimental phasing with native-SAD was carried out with SHELXC/D/E[30] via HKL2MAP
612 GUI[48] or with CRANK2 pipeline[31]. The mean peak height for anomalous data $\langle S_{anom} \rangle$ was
613 calculated using ANODE[49]. The structures were refined with phenix.refine[50] and deposited in
614 the Protein Data Bank (https://www.rcsb.org/).
615 **Sub-pixel uniformity characterization.** To explore the systematic errors of the detector on
616 the sub-pixel level, we group all the reflections according to where they impinge relative to a
617 pixel center. In this task we benefit from the fact that XDS provides the predicted reflection
618 center to a precision of 1/10th of a pixel. For each reflection we consider only the fractional
619 part of its position in-pixel units, ignoring its integer part. *e.g.*, if spot is predicted to fall in x
620 = 450.1 pixel and y = 363.5 pixel, we consider its "in-pixel position" as x = 1, y = 5. Since in
621 XDS the coordinate system in-pixel position x = 0, y = 0 corresponds to the center of a pixel,
622 we shift the positions by half pixel to put the origin of the coordinate system at a corner.
623 To quantify such spatial effect, we first calculate deviation from mean for each observation:
624 $$\Delta = \sqrt{\frac{n}{n-1}}(I_{obs} - \overline{I_{obs}}), \qquad (1)$$

where n is multiplicity, I_{obs} is measured intensity and $\overline{I_{obs}}$ is mean intensity for all symmetry equivalent reflections (including the one in question). The extra term $\sqrt{\frac{n}{n-1}}$ corrects for underestimation of the difference between observation and mean[51]. R_{meas} is then simply:

$$R_{meas} = \frac{\sum_{hkl}\sum_n |\Delta|}{\sum_{hkl}\sum_n \overline{I_{obs}}}, \quad (2)$$

where *n* is multiplicity. Reflections that were observed only once are ignored in the summation.

Next we bin all reflections according to their in-pixel position and for each position *x,y* we calculate:

$$\Delta_{x,y} = \sum_{hkl}\sum_n \Delta, \quad (3)$$

where *n* is the number of reflections that fall into a particular x,y in-pixel position. To allow comparison between in-pixel positions, $\Delta_{x,y}$ can be also normalized in a way similar to R-factors:

$$\Delta_{x,y}^{norm} = \frac{\Delta_{x,y}}{\sum_{hkl}\sum_n \overline{I_{obs}}}. \quad (4)$$

Since $\Delta_{x,y}^{norm}$ is calculated without taking the absolute value of $\Delta_{x,y}$ before averaging, random differences in intensity measurements should cancel out – a value close to zero of $\Delta_{x,y}^{norm}$ should indicate that there is no systematic error introduced at in-pixel position x,y. However, if reflections in a particular bin are systematically higher or smaller than the ones in other bins, $\Delta_{x,y}^{norm}$ should indicate it by a positive or negative value, respectively. $\Delta_{x,y}^{norm}$ values for each in-pixel position can then be presented on a map which indicates the degree of the non-uniformity across one pixel. The pixel maps calculated with low-resolution reflections (*d* > 10 Å) were presented in Fig. 5a-c.

With $\Delta_{x,y}$ in hand one can calculate the effect that charge sharing has on the R-factor value, by calculating the mean of the absolute values of $\Delta_{x,y}$:

$$R_{pxl} = \frac{\sum_{x,y}|\Delta_{x,y}|}{\sum_{hkl}\sum_n \overline{I_{obs}}}, \quad (5)$$

where N is the number of all reflections with multiplicity of at least two. Due to the fact that $|a| + |b| \geq |a + b|$, R_{meas} is an upper limit for R_{pxl} and comparison of the two values can indicate the share of systematic errors due to sub-pixel non-uniformity in relation to the total uncertainty.

For calculations we apply a standard cutoff for reflection intensities I > -3σ. Since we are interested in systematic deviations of reflection intensities, we also include misfits, marked in XDS_ASCII.HKL with negative σ values, in all statistics calculations presented in Fig. 5d-f (R_{pxl} and R_{meas}).

Photon count-rate estimation. Peak photon rate for a reflection observation was approximated as the following:

$$Rate = \frac{MAXC}{(0.075\ mm)^2} \frac{v}{\Delta\phi}, \quad (6)$$

where MAXC is the highest count observed in a single pixel from a single frame for a particular reflection (column MAXC in INTEGRATE.HKL from XDS), v is the rotation speed in °/s, Δϕ is the rotation range of a single image in degrees and 0.075 mm is the pixel pitch. This number is only the lower estimation of the peak rate, since while a crystal rotates, the intensity of a reflection varies according to its rocking curve, especially if Δϕ is larger than mosaicity (as in our case). However, if one compares data set collected with the same Δϕ, the incoming photon rate should be comparable in both. The spread in observed values might come from the different spread of counts inside a peak (charge sharing).

In Fig. 3d, we present correlations of peak rates of two JF1M data sets collected on the same crystal at 1°/s and 100°/s rotation speed with corresponding beam transmission of 1% and 100% (see above for exact experimental details). To ensure equivalent Δϕ frame summation was performed on the slower data set. For the correlation plot, we choose only reflections with identical Miller indices from both data sets, and no symmetry equivalence was applied. In this way, peak rates calculated in 1°/s JF1M data, multiplied by 100, is an approximation

of the "true" rates for 100°/s data. This is then compared with the measured rate values in 100°/s data.

For reference, we calculate peak rate values using a theoretical model for a paralyzable counter, where the relation between true count-rate I_0 and observed count-rate I is given as:

$$I = I_0 e^{-I_0 \tau}, \quad (7)$$

where τ is an energy dependent sensor dead-time. The τ value used in Fig. 3d was taken as 280 ns, which is an experimental value determined for 6 keV photons for the PSI manufactured EIGER[52].

Data availability

All diffraction data have been deposited in figshare depository and are accessible at https://doi.org/10.6084/m9.figshare.6087368. Diffraction data and refined models for native-SAD structures have been deposited in the Protein Data Bank under PDB identifiers 6G89 (thaumatin), 6G8A (lysozyme), and 6G8B (PepN).

Code availability

Custom computer code for pixel map and R_{pxl} calculations are available at https://github.com/fleon-psi/JF_analysis_scripts.

Online Methods References

42 Wojdyla, J. A. *et al.* DA+ data acquisition and analysis software at the Swiss Light Source macromolecular crystallography beamlines. *J Synchrotron Radiat* **25**, 293-303, doi:10.1107/s1600577517014503 (2018).

43 Redford, S. *et al.* Calibration status and plans for the charge integrating JUNGFRAU pixel detector for SwissFEL. *J Instrum* **11**, C11013-C11013, doi:10.1088/1748-0221/11/11/c11013 (2016).

44 Bernstein, H. J. & Hammersley, A. P. in *International Tables for Crystallography International Tables for Crystallography* Ch. Chapter 2.3, 37-43 (2006).

45 Peng, G. *et al.* Insight into the remarkable affinity and selectivity of the aminobenzosuberone scaffold for the M1 aminopeptidases family based on structure analysis. *Proteins: Structure, Function, and Bioinformatics* **85**, 1413-1421, doi:10.1002/prot.25301 (2017).

46 Paithankar, K. S., Owen, R. L. & Garman, E. F. Absorbed dose calculations for macromolecular crystals: improvements to RADDOSE. *J Synchrotron Radiat* **16**, 152-162, doi:10.1107/s0909049508040430 (2009).

47 Kabsch, W. XDS. *Acta Cryst* **D66**, 125-132, doi:10.1107/s0907444909047337 (2010).

48 Pape, T. & Schneider, T. R. HKL2MAP: a graphical user interface for macromolecular phasing withSHELXprograms. *Journal of Applied Crystallography* **37**, 843-844, doi:10.1107/s0021889804018047 (2004).

49 Thorn, A. & Sheldrick, G. M. ANODE: anomalous and heavy-atom density calculation. *Journal of Applied Crystallography* **44**, 1285-1287, doi:10.1107/s0021889811041768 (2011).

50 Afonine, P. V. *et al.* Towards automated crystallographic structure refinement with *phenix.refine*. *Acta Cryst* **D68**, 352-367, doi:10.1107/s0907444912001308 (2012).

51 Diederichs, K. & Karplus, P. A. Improved R-factors for diffraction data analysis in macromolecular crystallography. *Nat Struct Biol* **4**, 269-275 (1997).

52 Johnson, I. *et al.* Eiger: a single-photon counting x-ray detector. *J Instrum* **9**, C05032-C05032, doi:10.1088/1748-0221/9/05/c05032 (2014).

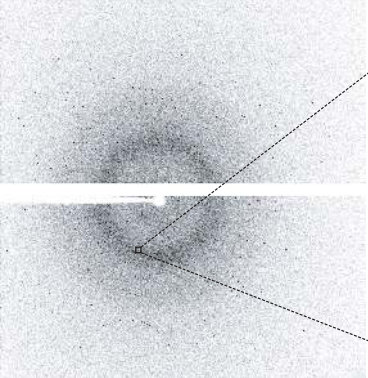

10	7	9	9	9	3	5	11
9	6	2	13	13	8	9	7
6	6	6	28	145	20	6	12
8	7	17	373	2384	77	14	9
6	11	13	211	312	19	6	9
4	7	10	11	12	12	11	5
6	5	8	6	12	7	9	11

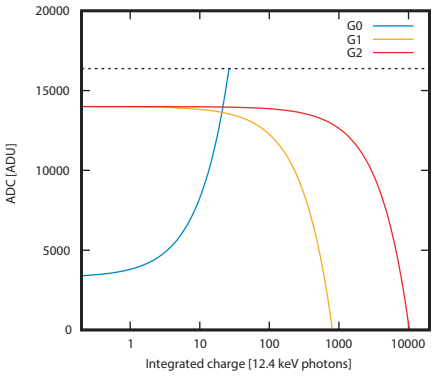

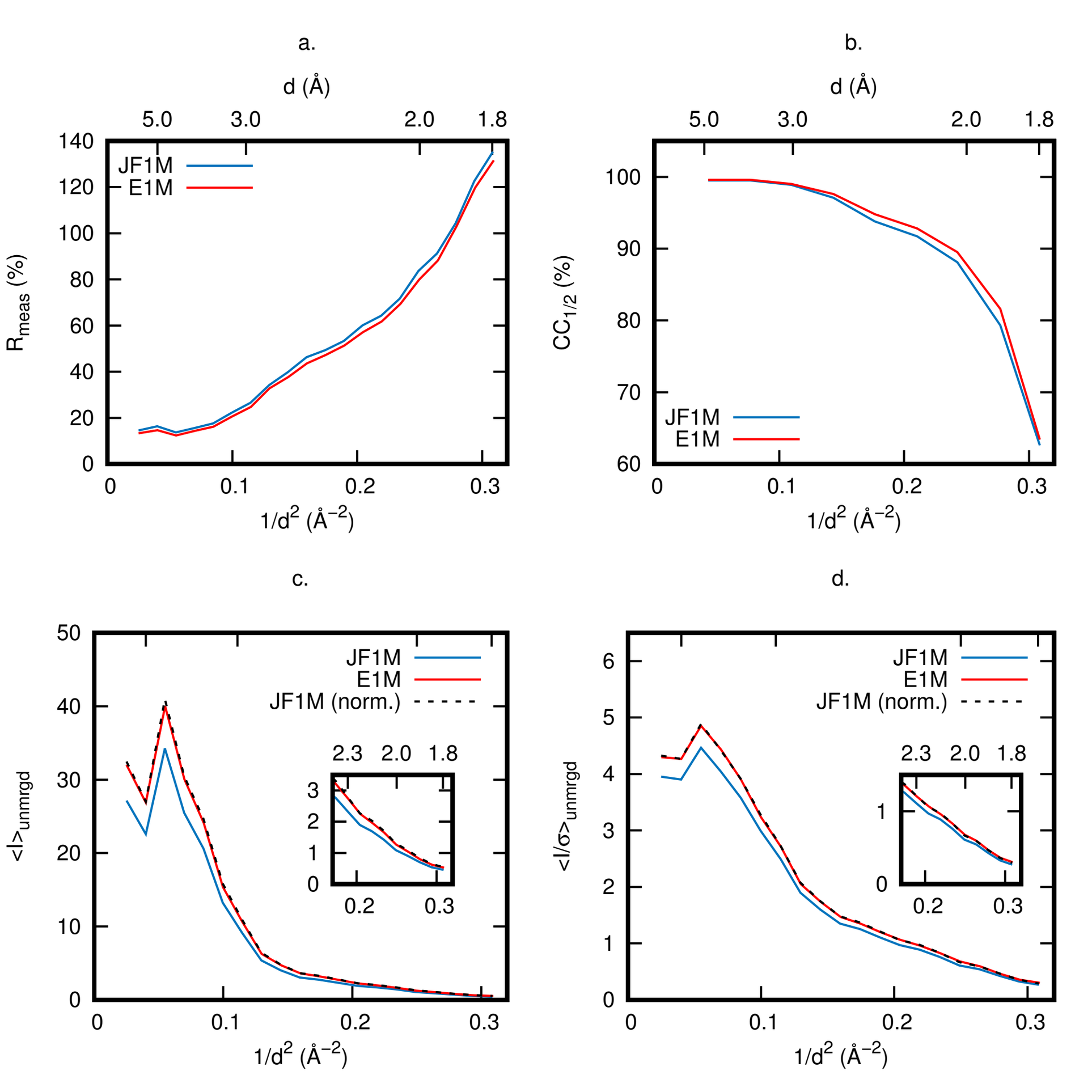
a.
d (Å)
5.0
3.0
2.0
1.8
JF1M
E1M
R_{meas} (%)
$1/d^2$ (Å^{-2})
b.
d (Å)
$CC_{1/2}$ (%)
$1/d^2$ (Å^{-2})
c.
JF1M (norm.)
$\langle I \rangle_{unmrgd}$
$1/d^2$ (Å^{-2})
d.
$\langle I/\sigma \rangle_{unmrgd}$
$1/d^2$ (Å^{-2})

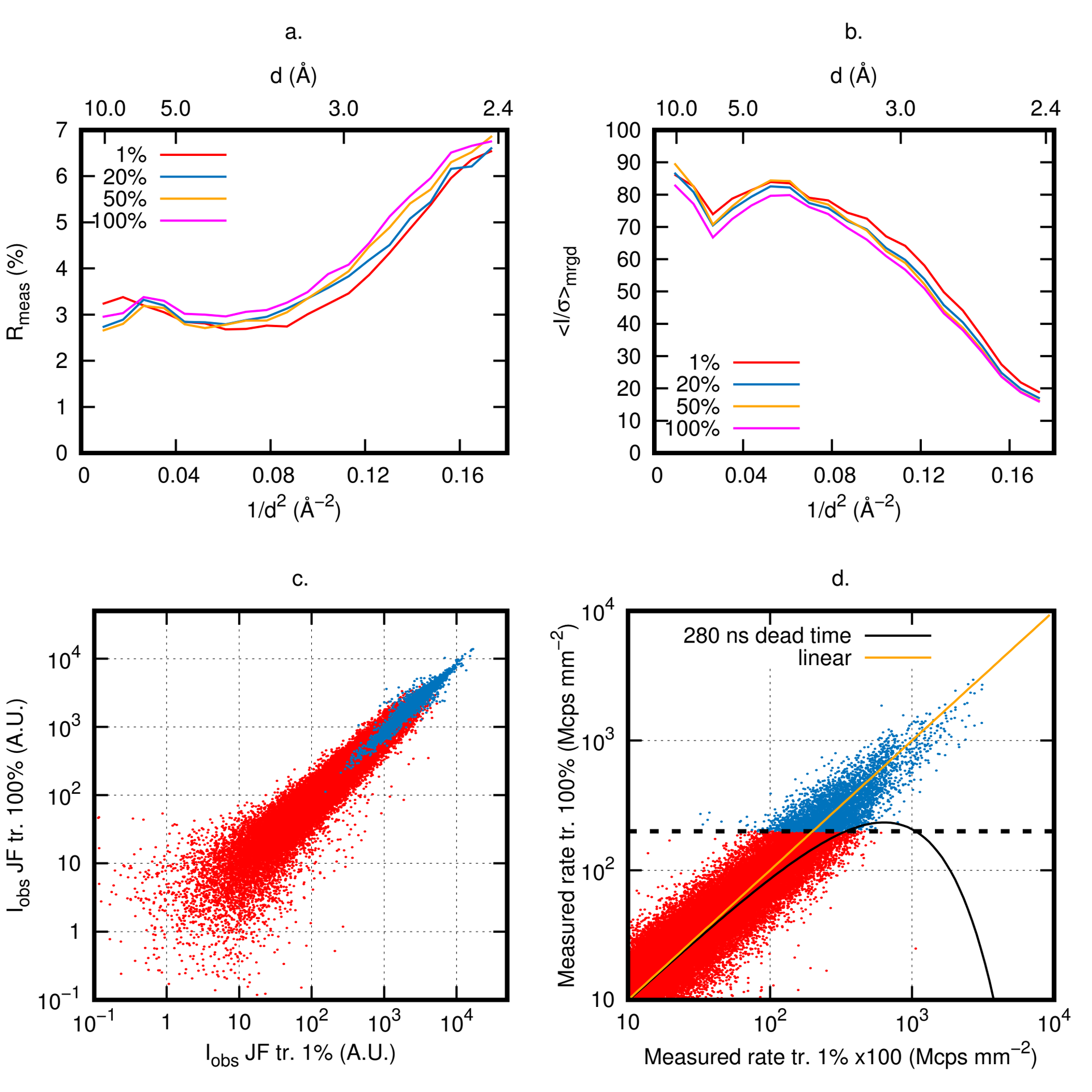
a.
d (Å)
10.0
5.0
3.0
2.4
1%
20%
50%
100%
R_{meas} (%)
$1/d^2$ (Å^{-2})
b.
d (Å)
10.0
5.0
3.0
2.4
1%
20%
50%
100%
$\langle I/\sigma \rangle_{mrgd}$
$1/d^2$ (Å^{-2})
c.
I_{obs} JF tr. 100% (A.U.)
I_{obs} JF tr. 1% (A.U.)
d.
280 ns dead time
linear
Measured rate tr. 100% (Mcps mm^{-2})
Measured rate tr. 1% x100 (Mcps mm^{-2})

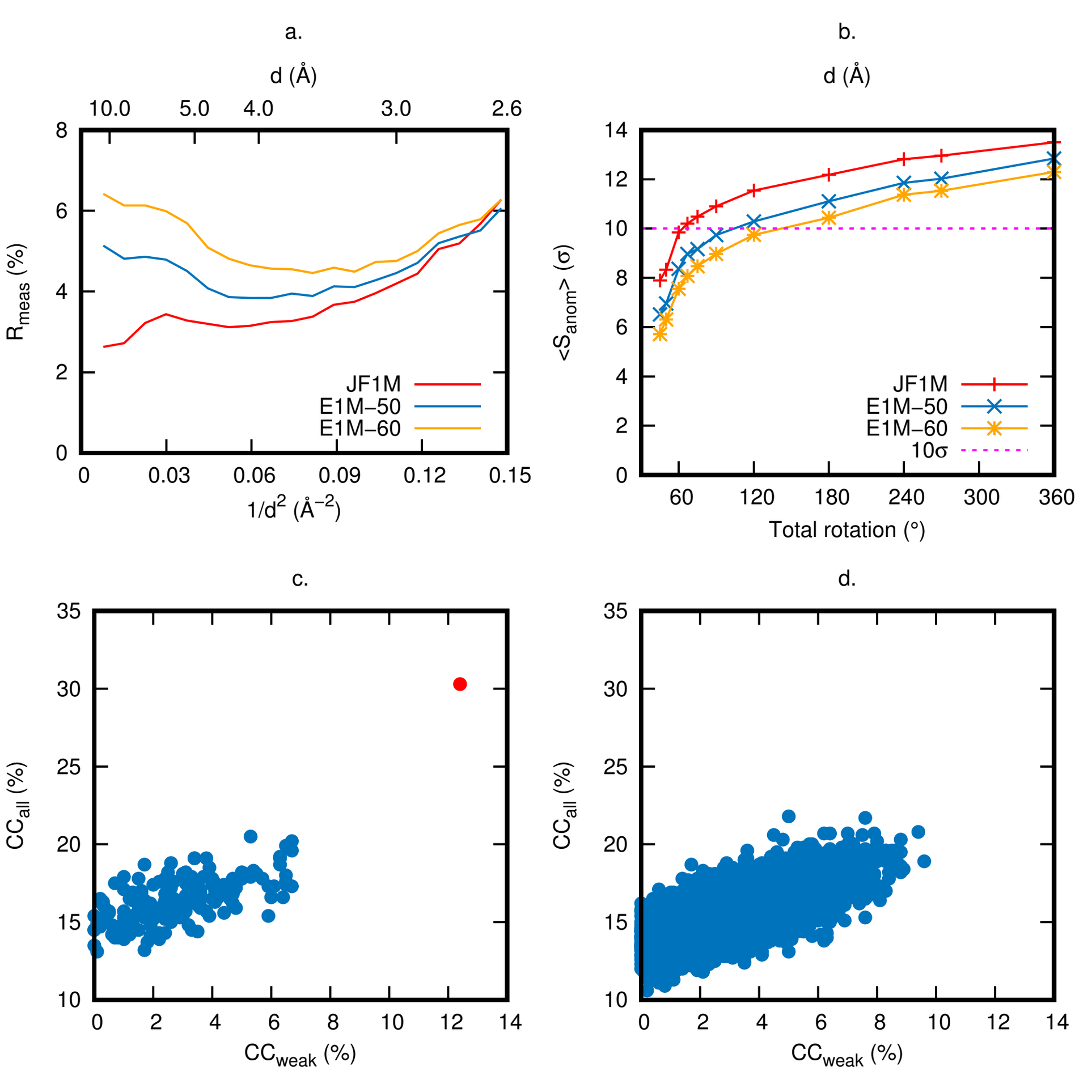
a.
d (Å)
10.0
5.0
4.0
3.0
2.6
8
6
4
2
0
0
0.03
0.06
0.09
0.12
0.15
R_{meas} (%)
$1/d^2$ (Å^{-2})
JF1M
E1M–50
E1M–60
b.
d (Å)
14
12
10
8
6
4
2
0
60
120
180
240
300
360
<S_{anom}> (σ)
Total rotation (°)
JF1M
E1M–50
E1M–60
10σ
c.
35
30
25
20
15
10
0
2
4
6
8
10
12
14
CC_{all} (%)
CC_{weak} (%)
d.
35
30
25
20
15
10
0
2
4
6
8
10
12
14
CC_{all} (%)
CC_{weak} (%)

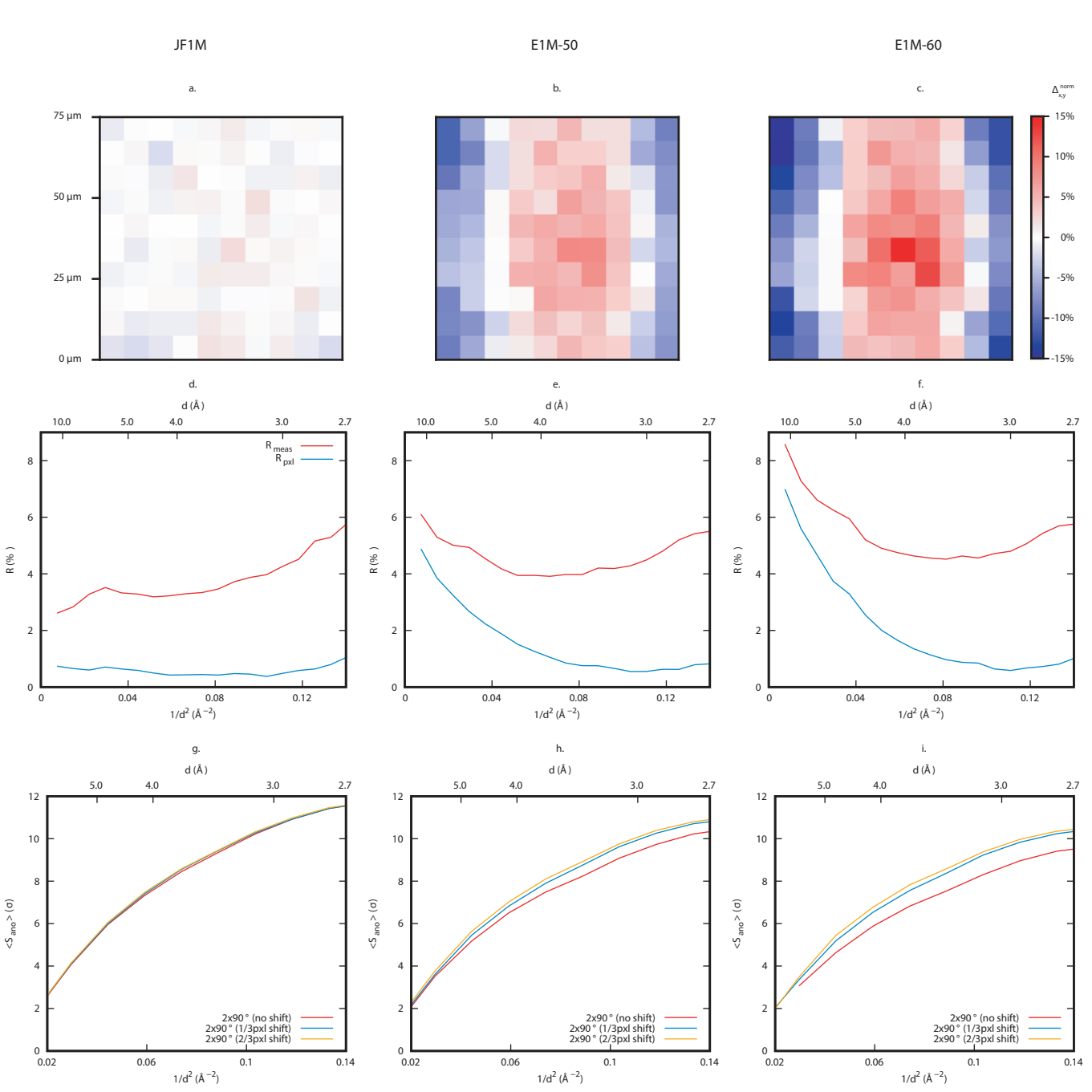
JF1M
E1M-50
E1M-60
a.
b.
c.
75 µm
50 µm
25 µm
0 µm
$\Delta_{x,y}^{norm}$
15%
10%
5%
0%
-5%
-10%
-15%
d.
e.
f.
d (Å)
10.0
5.0
4.0
3.0
2.7
R (%)
R_{meas}
R_{pxl}
0
2
4
6
8
0.04
0.08
0.12
$1/d^2$ (Å^{-2})
g.
h.
i.
$<S_{ano}>$ (σ)
0
2
4
6
8
10
12
0.02
0.06
0.1
0.14
2x90 ° (no shift)
2x90 ° (1/3pxl shift)
2x90 ° (2/3pxl shift)

a. Thaumatin (6 keV / 600 ms / 60 deg.)

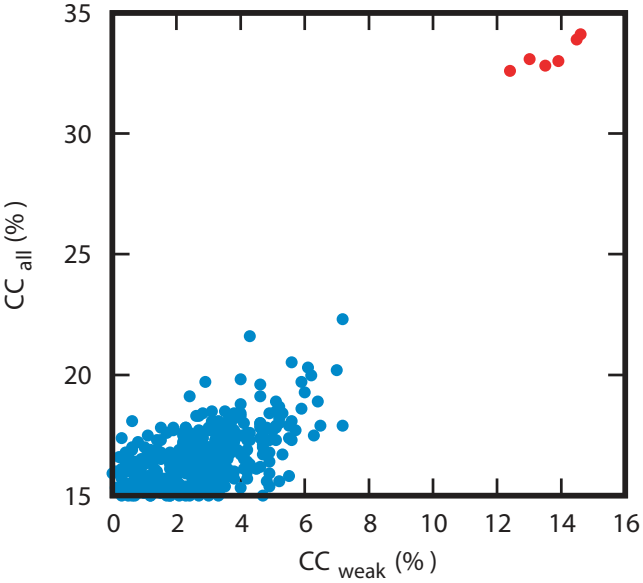

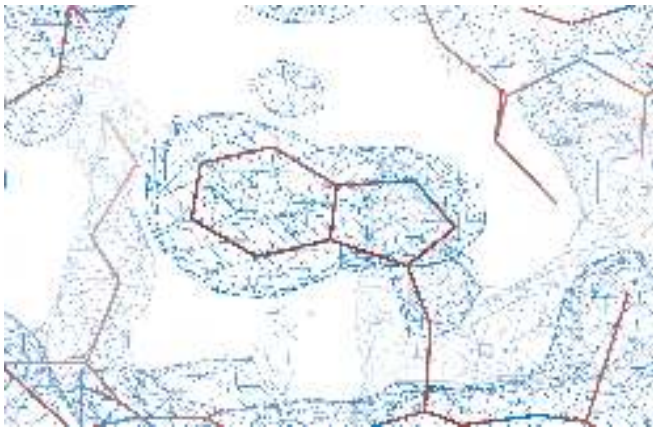

b. Lysozyme (12.4 keV / 5 sec / 500 deg.)

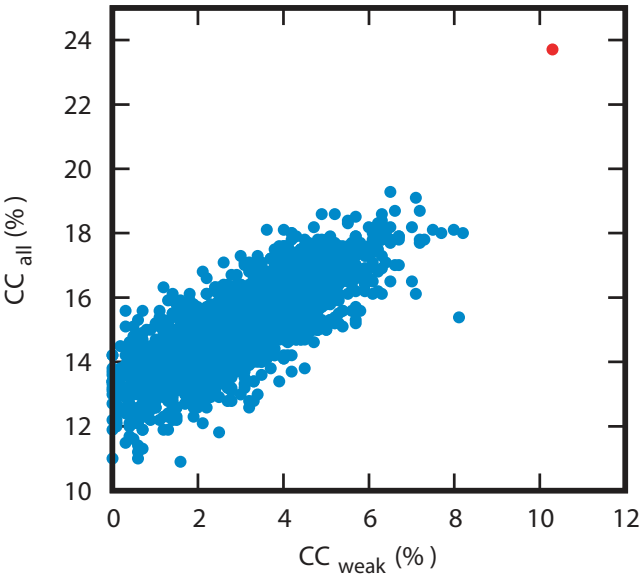

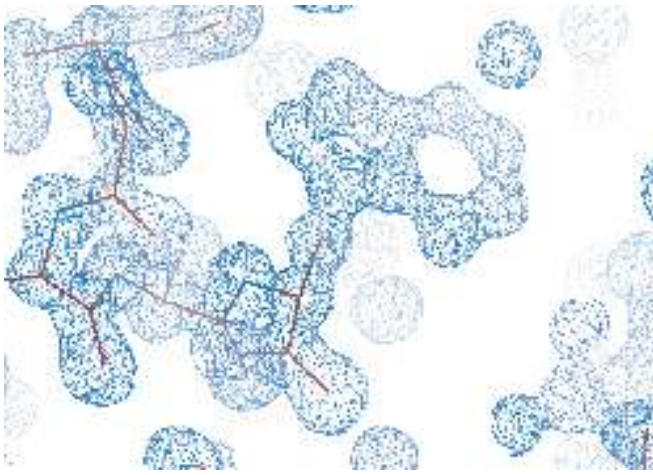

c. Aminopeptidase (6 keV / 60 sec / 600 deg.)